



Dynamical Spectral Unmixing of Multitemporal Hyperspectral Images

Simon Henrot, Jocelyn Chanussot, Christian Jutten

► To cite this version:

Simon Henrot, Jocelyn Chanussot, Christian Jutten. Dynamical Spectral Unmixing of Multitemporal Hyperspectral Images. IEEE Transactions on Image Processing, 2016, 25 (7), pp.3219 - 3232. 10.1109/TIP.2016.2562562 . hal-01346918

HAL Id: hal-01346918

<https://hal.science/hal-01346918>

Submitted on 19 Jul 2016

HAL is a multi-disciplinary open access archive for the deposit and dissemination of scientific research documents, whether they are published or not. The documents may come from teaching and research institutions in France or abroad, or from public or private research centers.

L'archive ouverte pluridisciplinaire **HAL**, est destinée au dépôt et à la diffusion de documents scientifiques de niveau recherche, publiés ou non, émanant des établissements d'enseignement et de recherche français ou étrangers, des laboratoires publics ou privés.

Dynamical spectral unmixing of multitemporal hyperspectral images

Simon Henrot, Jocelyn Chanussot, *Fellow, IEEE*, and Christian Jutten, *Fellow, IEEE*

Abstract—In this paper, we consider the problem of unmixing a time series of hyperspectral images. We propose a dynamical model based on linear mixing processes at each time instant. The spectral signatures and fractional abundances of the pure materials in the scene are seen as latent variables, and assumed to follow a general dynamical structure. Based on a simplified version of this model, we derive an efficient spectral unmixing algorithm to estimate the latent variables by performing alternating minimizations. The performance of the proposed approach is demonstrated on synthetic and real multitemporal hyperspectral images.

Index Terms—Hyperspectral imaging, Remote sensing, Source separation, Tensor decomposition

I. INTRODUCTION

Hyperspectral imaging consists in acquiring a set of images capturing a spatial scene at a few hundreds of wavelengths across the visible and near-infrared regions of the electromagnetic spectrum. The resulting data cube may equivalently be viewed as a set of two-dimensional (2D) gray-scale images, each corresponding to a particular spectral band, or as a collection of spectra, one per pixel of the image. In most cases, the image comprises a small number of pure materials, termed *endmembers* or *sources*, whose spectral signatures are mixed in each pixel. Spectral unmixing (SU) refers to the process of extracting the endmembers and estimating their corresponding mixing coefficients, or *abundances*, for each pixel in the image [1], [2].

In the *linear mixing model* (LMM), a given pixel spectrum \mathbf{x}^n in the image \mathbf{x} can be expressed as a linear combination of the pure spectra $\{\mathbf{s}^1, \dots, \mathbf{s}^P\}$, weighted by *abundance coefficients* \mathbf{a}^n representing the contribution of each source to \mathbf{x}^n :

$$\mathbf{x}^n = \mathbf{S} \mathbf{a}^n$$

where each column of matrix \mathbf{S} is a source spectrum, and n denotes the pixel index. In some cases, the mixing process is instead known to be nonlinear [3]. When incident light interacts with several endmembers before reaching the sensor (e.g. in *multilayered* configurations), the mixing process can be approximated as bilinear. When the mixing process occurs at a microscopic scale, the model exhibits a different type of nonlinearity [4]. In recent years, a number of papers have turned to a 'data-driven' approach to represent hyperspectral images in a high-dimensional manifold [5], [6], which has

the advantage of being robust over a wide range of mixing scenarios. The extent of nonlinear effects varies from a hyperspectral image to another, ranging from only a few pixels to the whole spatial scene. However, nonlinear SU methods typically exhibit a much higher computational complexity than their linear counterparts. Given the high dimensionality of hyperspectral data, the LMM remains widely used as the basis of many SU algorithms.

In many applications, sensors acquire the data at multiple time frames, yielding so-called *multitemporal* hyperspectral images. Multitemporal imaging allows to capture the dynamics of the underlying processes in the scene. The price to pay for this additional diversity is an even greater computational load, which gives an additional incentive to model the mixing process as linear for each time frame of the data. However, independently performing linear SU on each time frame is not sufficient. A first problem of this approach is the standard *permutation problem* which arises in blind source separation: the index of each extracted endmember changes from a time frame to another. More importantly, unmixing each time frame in a separate manner fails to exploit the temporal information in the data, and thus does not reach the true potential of multitemporal image processing.

Multitemporal hyperspectral imaging has garnered increasing interest in recent years, mainly focused on classification problems [7], [8]. For instance, working in a manifold-learning based framework allows to jointly process two time frames of the data by *aligning* the manifolds obtained at each time frame [9], [10], enabling the use of labels from a time frame to be transferred to another [11], [12]. Unfortunately, the resulting computational complexity can be a significant hurdle when processing many time frames.

Dedicated methods in the field of multitemporal spectral unmixing have only begun to emerge [13]. In this paper, we aim at providing a framework for modeling and efficient unmixing of a time series of hyperspectral images. Specifically, the main contribution of this paper is a model for multitemporal hyperspectral images, based on the LMM to retain the low complexity of linear SU methods. The temporal information in the data is accounted for by making assumptions on the dynamics of the underlying source spectra and abundance maps, seen as latent variables. Based on this model, we also propose an efficient SU algorithm which jointly processes all time frames in the image, and recovers source spectra and abundance maps fitting the proposed model. We demonstrate the performance of the proposed approach on real multitemporal hyperspectral images.

The remainder of the paper is organized as follows. In sec-

The authors are with GIPSA-lab/DIS, F-38402 Saint Martin d'Hères Cedex- France (e-mail: firstname.lastname@gipsa-lab.grenoble-inp.fr). Jocelyn Chanussot and Christian Jutten are also members of Institut Universitaire de France (IUF).

tion II, we introduce and discuss our model for multitemporal hyperspectral images. We derive a joint spectral unmixing algorithm in section III. The performances of the proposed approach are evaluated on synthetic and real multitemporal hyperspectral images in section IV. Finally, we conclude in section V.

II. PROPOSED MODEL FOR MULTITEMPORAL HYPERSPECTRAL IMAGES

Let $\mathbf{X} = \{\mathbf{X}_k, k \in \llbracket 1, K \rrbracket\}$ denote a time sequence of K hyperspectral images, where k is the discrete time index. Each image \mathbf{X}_k is encoded in a $L \times N$ matrix where L and N respectively (*resp.*) denote the number of wavelengths (*channels*) and the number of pixels in the image. In the following, \mathbf{x}_k^n denotes the n -th column of \mathbf{X}_k , *i.e.* the observed spectrum of the n -th pixel of image k , and similar notations are used for other matrices. Equations involving indices k, n, l, p will *resp.* hold for $k \in \llbracket 1, K \rrbracket, n \in \llbracket 1, N \rrbracket, l \in \llbracket 1, L \rrbracket, p \in \llbracket 1, P \rrbracket$ unless stated otherwise.

At each time k , we suppose that the standard linear mixing model holds, *i.e.* each pixel spectrum is obtained as a linear combination of P pure spectra or *sources* [2]:

$$\mathbf{X}_k = \mathbf{S}_k \mathbf{A}_k + \mathbf{E}_k \quad (1)$$

where $L \times P$ matrix \mathbf{S}_k gathers the spectral signatures of the P sources, and $P \times N$ abundance matrix \mathbf{A}_k contains the mixing coefficients. Matrix \mathbf{E}_k is an additive noise term which accounts for both measurements and model errors. The entries in $\mathbf{S} = \{\mathbf{S}_k\}$ and $\mathbf{A} = \{\mathbf{A}_k\}$ are known to be positive. The number of sources P is assumed to be known, *e.g.* using one of the methods presented in [14]–[16]. Since these methods are designed to be applied imagewise, their application will result in a vector of K values of P . The number of sources will be fixed as the maximum value of this vector. We will see later that the proposed model contains a parameter which allows to deal with the appearance or disappearance of a particular endmember.

The set of sources \mathbf{S} and their corresponding abundance coefficients \mathbf{A} may readily be obtained in a separate manner, that is, by running standard spectral unmixing algorithms at each time k . However, this approach may be viewed as flawed because it does not account for the dynamics of sources and abundance coefficients. Indeed, while the spectral signatures of sources extracted from the same spatial scenes at different times may not be strictly identical, we can expect them to bear some resemblance to each other. This similarity can be captured by modeling the dynamic *spectral variability* of the sources. Likewise, the abundance maps of sources extracted at neighboring time frames should be highly similar in most cases. In mathematical terms, we propose the following dynamic system:

$$\begin{cases} \mathbf{X}_k &= \mathbf{S}_k \mathbf{A}_k + \mathbf{E}_k \\ \mathbf{S}_k &= f_S(\mathbf{S}_{k-1}) + \mathbf{V}_k \\ \mathbf{A}_k &= f_A(\mathbf{A}_{k-1}) + \mathbf{D}_k \end{cases} \quad (2)$$

where functions f_S and f_A and noise terms \mathbf{E} , \mathbf{V} and \mathbf{D} must be tailored to the problem at hand. Since assumptions

are only made on the dynamics of the sources and abundance maps, rather than on the data themselves, our approach may be thought of as 'data-driven'.

We now propose a simplified version of (2) that is both general enough to encompass a wide range of situations and imaging scenarios, and tractable to accommodate the very large number of variables involved in multitemporal hyperspectral imaging.

The spectral shape of various instances of a source spectral signature is known to be mainly invariant [17]. Based on this rationale, [18] models the *spectral variability* of sources in the spatial dimension (from one pixel to another) by a scale change and an additive noise term. We propose here to use a similar model to characterize the spectral variability of sources in the temporal dimension:

$$\mathbf{s}_k^p = \psi_k^p \mathbf{s}_0^p + \mathbf{v}_k^p \quad (3)$$

where ψ_k^p is a (scalar) nonnegative scale factor, \mathbf{s}_0^p is the *reference* spectral signature for the p -th source and \mathbf{v}_k^p is a zero-mean additive noise term accounting for a nonlinear distortion. For each source, any of the following methods can be employed to obtain \mathbf{s}_0^p :

- selection in a dictionary when ground truth is available, or when the pure components in the image are known beforehand. Pruning methods may be applied to select the atoms of the dictionary [13];
- polynomial regression from a bundle of extracted spectra, if one wishes to compute average reference spectra;
- or simply setting the reference spectrum to the one extracted independently from the first image, *i.e.* $\mathbf{s}_0^p = \mathbf{s}_1^p$.

We make the important assumption that all images in the temporal sequence have been either acquired with a fixed sensor or coregistered beforehand, *e.g.* using methods based on cross-correlation [19]. Since each image is acquired over the same spatial scene, we assume that the abundance maps are given by

$$\mathbf{a}_k^n = \mathbf{a}_{k-1}^n + \mathbf{d}_k^n \quad (4)$$

where the noise term \mathbf{d}_k^n models a potential *change* in the spatial distribution (*e.g.* the replacement of a crop by another in agricultural remote sensing, or the displacement of a molecule within the medium in biological spectroscopy). Each entry \mathbf{d}_k^n is non-zero only if the abundance on the corresponding endmember changes in the pixel; hence, we assume that \mathbf{D}_k is sparse, and consequently \mathbf{D} too (see [20] for a similar assumption in the spatial dimension of the image).

Here, we choose not to enforce the common sum-to-one constraint on the abundances in order to preserve the flexibility of the algorithm, and expand the space to find an optimal solution. This is especially important when the endmembers can be impacted by a strong spectral variability. This gives also more flexibility regarding the estimation of the number of endmembers, if this number happens to be underestimated. Eventually, this has also an algorithmic positive side-effect, as simultaneously managing both the sum-to-one constraint on the columns of matrices \mathbf{A}_k and the sparse structure of the differences matrices \mathbf{D}_k is a challenging issue. Indeed, consider the case where the abundance of an endmember

changes in a pixel: $\mathbf{a}_{k-1}^n \neq \mathbf{a}_k^n$. Applying the sum-to-one constraint on the n -th column of \mathbf{A}_k forces the entire n -th column of \mathbf{D}_k to be non-zero. Considering the more general model without the sum-to-one constraint thus allows to bypass that issue.

Gathering (1), (3) and (4) in matrix form, we obtain the simplified dynamic system

$$\begin{cases} \mathbf{X}_k &= \mathbf{S}_k \mathbf{A}_k + \mathbf{E}_k \\ \mathbf{S}_k &= \mathbf{S}_0 \boldsymbol{\psi}_k + \mathbf{V}_k \\ \mathbf{A}_k &= \mathbf{A}_{k-1} + \mathbf{D}_k \end{cases} \quad (5)$$

where $\boldsymbol{\psi}_k$ is a diagonal matrix with the main diagonal gathering the values $(\psi_k^1, \dots, \psi_k^P)$.

In the next three subsections, we briefly consider the proposed model from different perspectives, in terms of potential links with the tensor decompositions and the standard state-space models. We then discuss the applicability of the approximation (5) to various real life datasets, in terms of acceptable limits on spectral invariability.

A. Similarity to tensor decompositions

Since $\underline{\mathbf{X}}$ is a tensor, model (5) can be viewed as a tensor decomposition. Specifically, if one cancels the additive noise term in (3), equations (5) and (3) combine to write

$$\mathbf{X}_k = \mathbf{S}_0 \boldsymbol{\psi}_k \mathbf{A}_k + \mathbf{E}_k \quad (6)$$

which is known as the *nonnegative tensor factorization 1* (NTF1) under nonnegativity constraints on \mathbf{S}_0 and $\underline{\mathbf{A}}$ [21]. Here, spectral variability is only accounted for by a varying scale factor at each time frame. Model (5) thus corresponds to a modified version of NTF1, which relaxes the factorization structure and imposes additional constraints on the dynamics on the abundance maps given by (4).

B. Similarity to state-space models

Another interpretation of model (5) lies in the framework of state-space representations. Here, observations $\underline{\mathbf{X}}$ are viewed as the output of a discrete time system with unknown internal states $\{\underline{\mathbf{S}}, \underline{\mathbf{A}}, \underline{\boldsymbol{\psi}}\}$. In control theory terms, the first equation of (5) would be referred to as the *measurement model*, and the second and third equations rewrite as *process models*:

$$\begin{cases} \mathbf{S}_k &= \mathbf{S}_{k-1} \hat{\boldsymbol{\psi}}_k + \hat{\mathbf{V}}_k \\ \mathbf{A}_k &= \mathbf{A}_{k-1} + \mathbf{D}_k \end{cases}$$

using straightforward recursive computations. Because the measurements $\underline{\mathbf{X}}$ and the update of $\underline{\mathbf{S}}$ are both bilinear functions of the state variables, standard Kalman filtering does not apply to the model. However, we will similarly aim at recovering the unknown variables $\{\underline{\mathbf{S}}, \underline{\mathbf{A}}, \underline{\boldsymbol{\psi}}\}$ based on the whole time series of images, rather than by considering single images [22].

C. Validity of the simplified dynamic system

A key assumption of the simplified model (5) is that endmembers have mainly invariant spectral shape. This is

a strong assumption, which works well *e.g.* when the data sequence is acquired with a high temporal resolution, as demonstrated in Section IV-B on images capturing the release of a gas plume. Other typical applications with high temporal resolution include sequences of multispectral images acquired in fluorescence microscopy / spectroscopy. In other practical applications such as seasonally varying vegetation over the course of weeks or months, the proposed model may not be valid and adjustments must be made to fit the underlying physical models. When crops are replaced with bare soil, for instance, one simple adjustment may consist in introducing an additional endmember in the model. If information on the seasonal \mathbf{S}_k 's is available via physical priors, the second equation of the model can be modified in a straightforward manner to allow variations around the nominal values instead of using a fixed matrix \mathbf{S}_0 . Additionally, other priors may be assumed on the difference matrices $\underline{\mathbf{D}}$ depending on the spatial layout of the crops.

As for spectral variations due to variable illumination and environmental, atmospheric and temporal conditions, more complex changes may be needed. In [23], the authors characterize methods accounting for spectral variability by either treating endmembers as sets or *bundles* of spectra, or as statistical distributions. If spectral variations of the endmembers belong to a known spectral library encoded in matrix \mathbf{S}_0 , one could extract the relevant spectral signatures at different time frames using a variation of the MESMA algorithm [24]. Another approach, belonging to the second class of methods, would consist in modeling each pixel as a linear combination of random endmembers following a Gaussian distribution as in [25]. Since deriving closed-form minimizers is difficult in this context, the optimization procedure would then require using a *Markov Chain Monte Carlo* approach which generates samples asymptotically distributed according to the joint posterior distribution of the unknown parameters. In both cases, one of the biggest challenges would consist in implementing efficient algorithms to deal with the high dimensionality of multitemporal hyperspectral images. We will see in the following section how it can be done in the context of the simplified model (5).

III. JOINT SPECTRAL UNMIXING

We propose to estimate the unknown variables as a minimizer of the following objective function:

$$\begin{aligned} \mathcal{J}(\underline{\mathbf{S}}, \underline{\mathbf{A}}, \underline{\boldsymbol{\psi}} | \underline{\mathbf{X}}) &= \frac{1}{2} \sum_{k=1}^K \|\mathbf{X}_k - \mathbf{S}_k \mathbf{A}_k\|_F^2 \\ &+ \frac{\lambda_S}{2} \sum_{k=1}^K \|\mathbf{S}_k - \mathbf{S}_0 \boldsymbol{\psi}_k\|_F^2 + \lambda_A \sum_{k=2}^K \|\mathbf{A}_k - \mathbf{A}_{k-1}\|_{\ell_1} \end{aligned} \quad (7)$$

where $\|\cdot\|_F$ and $\|\cdot\|_{\ell_1}$ resp. denote the Frobenius and ℓ_1 norm, and the notation $\mathcal{J}(\underline{\mathbf{S}}, \underline{\mathbf{A}}, \underline{\boldsymbol{\psi}} | \underline{\mathbf{X}})$ states that the objective function is minimized w.r.t. the unknown variables $\{\underline{\mathbf{S}}, \underline{\mathbf{A}}, \underline{\boldsymbol{\psi}}\}$ given the observations $\underline{\mathbf{X}}$. λ_S and λ_A are scalar regularization hyperparameters which control the weight of the different terms in (7). The first term in (7) measures the fitness of the

data to the model, and the second and third term allow to enforce the prior information of (5).

Before detailing our optimization strategy, we propose a way to set hyperparameters λ_S and λ_A in criterion (7) from a probabilistic standpoint.

A. Hyperparameter tuning

In a Bayesian framework, criterion (7) may be viewed as the *maximum a posteriori* (MAP) estimator of the unknown variables $\{\underline{\mathbf{S}}, \underline{\mathbf{A}}, \underline{\psi}\}$ given the observations $\underline{\mathbf{X}}$. Hence, by making the following assumptions

- 1) all entries of tensor $\underline{\mathbf{E}}$ are i.i.d. centered Gaussian random variables of variance σ_e^2 ;
- 2) all entries of tensor $\underline{\mathbf{V}}$ are i.i.d. centered Gaussian random variables of variance σ_v^2 ;
- 3) all entries of tensor $\underline{\mathbf{W}}$ are i.i.d. centered Laplacian random variables of scale b ,

standard computations yield the following values:

$$\begin{cases} \lambda_S &= \sigma_e^2 / \sigma_v^2 \\ \lambda_A &= \sigma_e^2 / b. \end{cases} \quad (8)$$

Equation (8) allows to set parameters λ_S and λ_A providing σ_e , σ_v and b are known or can be estimated from the data set at hand. When this is not the case, λ_S and λ_A can be estimated using the approach recently proposed in [26], or by a sub-optimal strategy of trial and error.

In the next section, we detail an optimization procedure to minimize this criterion.

B. Optimization

Since the number of variables involved is very large, we propose to minimize (7) using an *projected alternated least squares* strategy or *alternating nonnegative least squares* (ANLS) [27] similarly to the approach of [28]. The method consists in alternatively solving the following problems

$$\begin{cases} \min_{\underline{\mathbf{S}}} \mathcal{J}(\underline{\mathbf{S}}, \underline{\mathbf{A}}, \underline{\psi}; \lambda_A, \lambda_S) \text{ s.t. } \underline{\mathbf{S}} \geq 0 \\ \min_{\underline{\mathbf{A}}} \mathcal{J}(\underline{\mathbf{S}}, \underline{\mathbf{A}}, \underline{\psi}; \lambda_A, \lambda_S) \text{ s.t. } \underline{\mathbf{A}} \geq 0 \\ \min_{\underline{\psi}} \mathcal{J}(\underline{\mathbf{S}}, \underline{\mathbf{A}}, \underline{\psi}; \lambda_A, \lambda_S) \end{cases} \quad (9)$$

until some stopping criterion is satisfied. We now detail the resolution of each subproblem.

1) *Minimization w.r.t. $\underline{\mathbf{S}}$* : We use the *Alternated Direction Method of Multipliers* (ADMM) [29] to tackle the nonnegativity constraints, in which the minimization of (7) w.r.t. $\{\mathbf{S}_k, k = 1, \dots, K\}$ is rewritten using a set $\underline{\mathbf{M}}$ of auxiliary matrices $\{\mathbf{M}_k, k = 1, \dots, K\}$ of size $L \times P$:

$$\begin{aligned} \min_{\underline{\mathbf{S}}, \underline{\mathbf{M}}} \sum_{k=1}^K \frac{1}{2} \left(\|\mathbf{X}_k - \mathbf{S}_k \mathbf{A}_k\|_F^2 + \frac{\lambda_S}{2} \sum_{k=1}^K \|\mathbf{S}_k - \mathbf{S}_0 \psi_k\|_F^2 \right. \\ \left. + I_{(\mathbb{R}^+)^{L \times P}}(\mathbf{M}_k) \right) \\ \text{s.t. } \mathbf{S}_k - \mathbf{M}_k = \mathbf{0}, k \in \{1, \dots, K\} \end{aligned} \quad (10)$$

where $I_{(\mathbb{R}^+)^{L \times P}}$ denotes the indicator function of the positive orthant of $\mathbb{R}^{L \times P}$. The augmented Lagrangian of the problem

is given by

$$\begin{aligned} \mathcal{L}_\rho = \sum_{k=1}^K \frac{1}{2} \left(\|\mathbf{X}_k - \mathbf{S}_k \mathbf{A}_k\|_F^2 + \frac{\lambda_S}{2} \sum_{k=1}^K \|\mathbf{S}_k - \mathbf{S}_0 \psi_k\|_F^2 \right. \\ \left. + I_{(\mathbb{R}^+)^{L \times P}}(\mathbf{M}_k) + \frac{\rho}{2} \|\mathbf{S}_k - \mathbf{M}_k + \mathbf{U}_k\|_2^2 - \frac{\rho}{2} \|\mathbf{U}_k\|_F^2 \right) \end{aligned} \quad (11)$$

where ρ is called the *barrier parameter* and $\underline{\mathbf{U}} = \{\mathbf{U}_k, k = 1, \dots, K\}$ are the so-called *normalized Lagrange multipliers*, which are scaled by a factor of ρ so that the augmented Lagrangian only incorporates quadratic terms. The procedure then consists in alternatively minimizing \mathcal{L}_ρ w.r.t. $\underline{\mathbf{S}}$ and $\underline{\mathbf{M}}$ and updating the normalized Lagrange multipliers $\underline{\mathbf{U}}$ (*dual update*), until the stopping criteria based on the primal and dual residuals are satisfied [29]. The minimization w.r.t. $\underline{\mathbf{S}}$ is performed by canceling the gradients of \mathcal{L}_ρ , while the minimization w.r.t. $\underline{\mathbf{M}}$ uses the frameworks of *proximal operators*¹ and the dual update consists in maximizing the dual problem w.r.t. $\underline{\mathbf{U}}$:

$$\begin{cases} \mathbf{S}_k &\leftarrow (\mathbf{X}_k \mathbf{A}_k^T + \lambda_S \mathbf{S}_0 \psi_k + \rho(\mathbf{M}_k - \mathbf{U}_k)) \\ &(\mathbf{A}_k \mathbf{A}_k^T + (\lambda_S + \rho) \mathbf{I}_P)^{-1} \\ \mathbf{M}_k &\leftarrow \Pi_{(\mathbb{R}^+)^{L \times P}}(\mathbf{S}_k + \mathbf{U}_k) \\ \mathbf{U}_K &\leftarrow \mathbf{U}_k + \mathbf{S}_k - \mathbf{M}_k \end{cases} \quad (12)$$

where \mathbf{I}_P is the $P \times P$ identity matrix and the projector onto $(\mathbb{R}^+)^{L \times P}$, denoted by $\Pi_{(\mathbb{R}^+)^{L \times P}}$, is the proximal operator of $I_{(\mathbb{R}^+)^{L \times P}}$. Note that all updates have a closed-form expression and the computational complexity is dominated by cheap inversions of $P \times P$ matrices.

2) *Minimization w.r.t. $\underline{\mathbf{A}}$* : Likewise, the ℓ_1 penalty term suggests the use of the ADMM. We introduce two sets of auxiliary matrices: $\{\mathbf{Q}_k, k = 1, \dots, K\}$ of size $P \times N$ and $\{\mathbf{D}_k, k = 2, \dots, K\}$ of size $P \times N$ and rewrite the problem as

$$\begin{aligned} \min_{\underline{\mathbf{A}}, \underline{\mathbf{D}}, \underline{\mathbf{Q}}} \sum_{k=1}^K \frac{1}{2} \left(\|\mathbf{X}_k - \mathbf{S}_k \mathbf{A}_k\|_F^2 + I_{(\mathbb{R}^+)^{P \times N}}(\mathbf{Q}_k) \right) \\ + \lambda_A \sum_{k=2}^K \|\mathbf{D}_k\|_{\ell_1} \\ \text{s.t. } \mathbf{A}_k - \mathbf{A}_{k-1} - \mathbf{D}_k = \mathbf{0}, k \in \{2, \dots, K\} \\ \text{s.t. } \mathbf{A}_k - \mathbf{Q}_k = \mathbf{0}, k \in \{1, \dots, K\}. \end{aligned} \quad (13)$$

The augmented Lagrangian of the problem is

$$\begin{aligned} \mathcal{L}_\rho = \sum_{k=1}^K \frac{1}{2} \left(\|\mathbf{X}_k - \mathbf{S}_k \mathbf{A}_k\|_F^2 + I_{(\mathbb{R}^+)^{P \times N}}(\mathbf{Q}_k) \right. \\ \left. + \frac{\rho}{2} \|\mathbf{A}_k - \mathbf{Q}_k + \mathbf{W}_k\|_2^2 - \frac{\rho}{2} \|\mathbf{W}_k\|_F^2 \right) \\ + \sum_{k=2}^K \left(\lambda_A \|\mathbf{D}_k\|_{\ell_1} + \frac{\rho}{2} \|\mathbf{A}_k - \mathbf{A}_{k-1} - \mathbf{D}_k + \mathbf{Z}_k\|_2^2 - \frac{\rho}{2} \|\mathbf{Z}_k\|_F^2 \right) \end{aligned} \quad (14)$$

¹The *proximal operator* of a function h with penalty ρ is defined as

$$\text{prox}_{h, \rho}(t) \triangleq \arg \min_z \{h(z) + (\rho/2)(z - t)^2\}.$$

where $\underline{\mathbf{W}}$ and $\underline{\mathbf{Z}}$ are the normalized Lagrange multipliers associated to both sets of constraints. The procedure is similar to the one exposed in the previous section and yields the following updates w.r.t. $\underline{\mathbf{A}}$:

$$\begin{cases} \mathbf{A}_1 \leftarrow (\mathbf{S}_1^t \mathbf{S}_1 + 2\rho \mathbf{I}_P)^{-1} (\mathbf{S}_1^t \mathbf{X}_1 + \rho(\mathbf{A}_2 - \mathbf{D}_2 + \mathbf{Z}_2 + \mathbf{Q}_1 - \mathbf{W}_1)) \\ \mathbf{A}_k \leftarrow (\mathbf{S}_k^t \mathbf{S}_k + 3\rho \mathbf{I}_P)^{-1} (\mathbf{S}_k^t \mathbf{X}_k + \rho(\mathbf{A}_{k+1} + \mathbf{A}_{k-1} - \mathbf{D}_{k+1} + \mathbf{D}_k + \mathbf{Z}_{k+1} - \mathbf{Z}_k + \mathbf{Q}_k - \mathbf{W}_k)), k \in \{2 \dots K-1\} \\ \mathbf{A}_K \leftarrow (\mathbf{S}_K^t \mathbf{S}_K + 2\rho \mathbf{I}_P)^{-1} (\mathbf{S}_K^t \mathbf{X}_K + \rho(\mathbf{A}_{K-1} + \mathbf{D}_K - \mathbf{Z}_K + \mathbf{Q}_K - \mathbf{W}_K)). \end{cases} \quad (15)$$

Recalling that the proximal operator of the absolute value is the *soft-thresholding* operator, the updates w.r.t. $\underline{\mathbf{D}}$ and $\underline{\mathbf{Q}}$ are:

$$\begin{cases} \mathbf{Q}_k \leftarrow \Pi_{(\mathbb{R}^+)^{P \times N}}(\mathbf{A}_k + \mathbf{W}_k), k \in \{1, \dots, K\} \\ \mathbf{D}_k \leftarrow \max(\mathbf{A}_k - \mathbf{A}_{k-1} + \mathbf{U}_k - \lambda_A/\rho, 0) \\ \quad - \max(-\mathbf{A}_k + \mathbf{A}_{k-1} - \mathbf{U}_k - \lambda_A/\rho, 0), k \in \{2, \dots, K\}. \end{cases} \quad (16)$$

Finally, the dual updates are given by

$$\begin{cases} \mathbf{W}_k \leftarrow \mathbf{W}_k + \mathbf{A}_k - \mathbf{Q}_k, k \in \{1, \dots, K\} \\ \mathbf{Z}_k \leftarrow \mathbf{Z}_k + \mathbf{A}_k - \mathbf{A}_{k-1} - \mathbf{D}_k, k \in \{2, \dots, K\}. \end{cases} \quad (17)$$

Again, the computational complexity of all involved operations is very low.

3) *Minimization w.r.t. $\underline{\psi}$* : Since ψ_k is a diagonal matrix, we only need to update the diagonal coefficients. The gradient of criterion (7) w.r.t. coefficient ψ_k^p is given by

$$\frac{\partial \mathcal{J}}{\partial \psi_k^p} = (\mathbf{s}_0^p)' \mathbf{s}_0^p \psi_k^p - (\mathbf{s}_0^p)' \mathbf{s}_k^p \quad (18)$$

hence, the update rule is

$$\psi_k^p \leftarrow \frac{(\mathbf{s}_0^p)' \mathbf{s}_k^p}{(\mathbf{s}_0^p)' \mathbf{s}_0^p}. \quad (19)$$

Note that this update guarantees the nonnegativity of coefficients $\{\psi_k, k = 1, \dots, K\}$. It is worth noting at this point that the algorithm only iterates closed-form updates for all variables of interest. The method is summarized in the next section.

C. Algorithm outline

Initialization of the unknown matrices $\{\mathbf{S}_k, \mathbf{A}_k, k = 1, \dots, K\}$ can easily be carried out in a separate fashion, *e.g.* using *Vertex Component Analysis* (VCA) [30] or *Minimum Volume Simplex Analysis* (MVSA) [31], and *Fully Constrained Least Squares* (FCLS) [32]. The algorithm structure is displayed in table I.

Data: $\{\mathbf{X}_k, k = 1, \dots, K\}$
Result: $\{\mathbf{S}_k, \mathbf{A}_k, \psi_k, k = 1, \dots, K\}$
 Set $\lambda_A, \lambda_S, \epsilon_S, \epsilon_A, \underline{\mathbf{S}}^{\text{init}}, \underline{\mathbf{A}}^{\text{init}}, \underline{\psi}^{\text{init}},$

```

repeat
  repeat
    Compute  $\underline{\mathbf{S}}^{\text{new}}, \underline{\mathbf{M}}^{\text{new}}$  and  $\underline{\mathbf{U}}^{\text{new}}$  using (12);
  until ADMM stopping criterion is satisfied;
  repeat
    Compute  $\underline{\mathbf{A}}^{\text{new}}$  using (15);
    Compute  $\underline{\mathbf{D}}^{\text{new}}$  and  $\underline{\mathbf{Q}}^{\text{new}}$  using (16);
    Compute  $\underline{\mathbf{W}}^{\text{new}}$  and  $\underline{\mathbf{Z}}^{\text{new}}$  using (17);
  until ADMM stopping criterion is satisfied;
  Compute  $\underline{\psi}^{\text{new}}$  using (19);
until ALS stopping criterion is satisfied;

```

Algorithm 1: Joint spectral unmixing of multi-temporal images

TABLE I
PROPOSED METHOD FOR JOINTLY UNMIXING HYPERSPECTRAL MULTITEMPORAL IMAGES.

D. Remarks on the convergence of the method

We propose the following stopping criteria:

$$\frac{\sum_{k=1}^K \|\mathbf{A}_k^{\text{new}} - \mathbf{A}_k\|_F^2}{\sum_{k=1}^K \|\mathbf{A}_k\|_F^2} < \epsilon_A \quad (20)$$

$$\frac{\sum_{k=1}^K \|\mathbf{S}_k^{\text{new}} - \mathbf{S}_k\|_F^2}{\sum_{k=1}^K \|\mathbf{S}_k\|_F^2} < \epsilon_S, \quad (21)$$

i.e. the optimization stops when the residuals on $\underline{\mathbf{S}}$ and $\underline{\mathbf{A}}$ are sufficiently small.

The optimization problem falls in the general class of *Non-negative Matrix Factorization* (NMF) problems, which are non convex and typically have local minima and non-uniqueness issues. Indeed, the objective function is convex w.r.t. each set of unknown variables $\{\underline{\mathbf{S}}, \underline{\mathbf{A}}, \underline{\psi}\}$ but it is not jointly convex. However, it is well known that the incorporation of additional constraints into the NMF model is a way to obtain a more well-posed NMF problem [33]. For instance, it has been shown that the non-negative problem admits a unique solution under well formulated conditions [34]. While theoretical guarantees are out of the scope of this paper, the two regularization terms in (7) also help constraining the range of admissible solutions. This is confirmed by our experimental results, presented in the following section.

The sub-problems are tackled using the ADMM algorithm to deal with the nonnegativity constraints. We use the standard stopping criteria proposed in [29] for each ADMM step. Since the ADMM steps only provide approximated minimizers of the sub-problems, only convergence to stationary points can be 'approximately' guaranteed.

IV. EXPERIMENTAL RESULTS

In this section, we evaluate the performance of the proposed method, thereafter called 'joint unmixing'. We compare it to a 'separate unmixing' approach where each time frame is processed separately by first extracting endmembers using VCA [18] or MVSA [31], then estimating abundances using SUNSAL [35]. The comparison metric is the scaled mean square error (MSE), defined by

$$\begin{aligned} e_A &= \frac{\sum_{k=1}^K \|\mathbf{A}_k^{\text{est}} - \mathbf{A}_k^{\text{true}}\|_F^2}{\sum_{k=1}^K \|\mathbf{A}_k^{\text{true}}\|_F^2} \\ e_S &= \frac{\sum_{k=1}^K \|\mathbf{S}_k^{\text{est}} - \mathbf{S}_k^{\text{true}}\|_F^2}{\sum_{k=1}^K \|\mathbf{S}_k^{\text{true}}\|_F^2}. \end{aligned} \quad (22)$$

A. Experiments on synthetic data

We consider a synthetic time series of ten hyperspectral images, composed of three endmembers. First, we design an abundance map for the first frame composed of three overlapping circular regions. Three real spectra corresponding to various gases are randomly picked from a dictionary (see next section), sampled on 129 wavelengths. We set spectral scale factors as one period of a sinusoid over the ten time frames. Model (5) is then applied based on the first image to create a time series of hyperspectral images, using sparse perturbation matrices \mathbf{D} generated using Laplacian distributions with $\sigma_e = \sigma_v = 5e^{-2}$ and $b = 1e^{-2}$ (these parameters are assumed to be known in these experiments).

In the case of separate unmixing, we compare the results yielded by VCA and MVSA, by testing values of the tuning parameters (spherization parameter and maximum eigenvalue of the quadratic approximation term) discretized on 15 points on a logarithmic scale from 10^{-10} to 10^4 and selecting the best score in each case. Since the true abundance maps contain pure pixels, VCA produced the best estimates of the endmembers in the mean square error (MSE) sense. Likewise, the impact of several values of the regularization parameter of SUNSAL was tested with a similar scheme. The resulting sources are sorted out by minimizing the spectral angle distance between the estimated matrix and matrix \mathbf{S}_0 over all possible permutations. In the case of joint unmixing, the algorithm is initialized by unity scale factors and constant abundance maps and \mathbf{S}_0 is fixed to the true endmember matrix. Note that here, contrarily to the separate unmixing approach, the proposed algorithm does not suffer from the permutation ambiguity: that is, the structure of the problem forces the index for each physical source to be the same at each time frame. Hyperparameters λ_S and λ_A are set using the probabilistic interpretation of section III-A.

We then compare the separate and joint unmixing approach on this data set; results are displayed for the tenth time frame in figure 2. Visually, both methods seem to give similar performances; thus, we turn to a quantitative measure to compare the two algorithms. We run the comparison for ten different noise trials and two different scenarios, \mathcal{S}_1 and \mathcal{S}_2 , related to two different endmember matrices \mathbf{S}_0 :

- (\mathcal{S}_1): the true endmember matrix \mathbf{S}_0 is assumed to be known beforehand ;

- (\mathcal{S}_2): \mathbf{S}_0 is assumed to be unknown and is set to the endmembers extracted by the separate unmixing approach applied to the first image.

The mean scaled MSEs of the estimated spectra and abundance maps reveal that joint unmixing outperforms separate unmixing, as shown in table II.

Figure 1 displays the estimated scale factors (represented as crosses; true values are indicated as straight lines). The scaled MSE value of the scale factors estimate is very low, at 0.02 and the good estimation performance is confirmed by the visual plots. The simulation thus shows that the proposed method can produce good estimates of the scale factors, even with no prior knowledge on their values. The next step then consists in applying the algorithm to a real data set.

B. Experiments on real data

In this section, we evaluate the performance of the proposed approach on *longwave infrared* (LWIR) spectroscopy data. LWIR imaging allows to capture a scene based on thermal emissions only, requiring no illumination. The scene of interest was acquired in a desert in 2006 [36], and captures a chemical gas plume emitted from a specific location. Specifically, we focus on a time series of hyperspectral images observed by a Fourier-Transform (FTIR) sensor located 2.82km from the release ground. We consider twelve time frames, which account for the dynamics of the release of the gas plume. The first time instant is taken just before the release, and the subsequent eleven frames cover the early gas emission. Each hyperspectral data cube comprises 128×320 spatial pixels and 129 wavelengths taken with a 4 cm^{-1} frequency spacing. The first principal component of each time frame is displayed in figure 4.

In this scene, we expect multiple scattering effects to take place in the spatial support of the gas plume. To verify this, we perform nonlinear detection on the pixels of the third time frame, using the method presented in [37]. The first step consists in carrying out nonlinear unmixing on the image. In this approach, each pixel in the image is given by the *polynomial post-nonlinear mixing model* (PPNMM) [37]:

$$\mathbf{x}_k^n = \mathbf{S}_k \mathbf{a}_k^n + b_k^n (\mathbf{S}_k \mathbf{a}_k^n) \odot (\mathbf{S}_k \mathbf{a}_k^n) + \mathbf{e}_k^n \quad (23)$$

where \odot stands for the Hadamard (entry-wise) product, and the nonlinear term is scaled by the scalar parameter b_k^n . In other words, b_k^n quantifies the nonlinearity of the mixing process for each pixel in the image, and the PPNMM reduces to the LMM for $\mathbf{B} = \mathbf{0}$. The nonlinearity parameter is estimated for each pixel in the image and a general likelihood ratio test is then used on \mathbf{B} to decide whether each pixel results from the LMM or the PPNMM. Figure 3 displays the decision for each pixel of the third time frame, with the false alarm probability set as 0.05. As expected, the mixing process is mostly nonlinear within the spatial support of the gas plume only (isolated pixels appearing on the map correspond to remaining outliers). Hence, we expect traditional unmixing methods to fail in this specific area.

We preprocess the data to filter out outliers caused by defaults in the sensor. First, their location is determined by

	Running time	mean(e_S)	std(e_S)	mean(e_A)	std(e_A)
Separate unmixing	15 sec	0.95	0.03	1.11	0.03
Joint unmixing (S_1)	18 min	0.63	0.02	0.66	0.01
Joint unmixing (S_2)	16 min	0.79	0.08	0.87	0.08

TABLE II

MEAN AND STANDARD DEVIATIONS (DENOTED BY 'STD') OF THE SCALED MEAN SQUARE ERRORS OF THE ESTIMATED SPECTRA AND ABUNDANCE MAPS, RESPECTIVELY DENOTED BY e_S AND e_A , DEFINED BY EQUATION (22). IN THE JOINT UNMIXING APPROACH, THE ENDMEMBER MATRIX S_1 IS EITHER ASSUMED TO BE KNOWN BEFOREHAND (S_1) OR SET TO THE ENDMEMBERS EXTRACTED BY THE SEPARATE UNMIXING APPROACH APPLIED TO THE FIRST IMAGE (S_2).

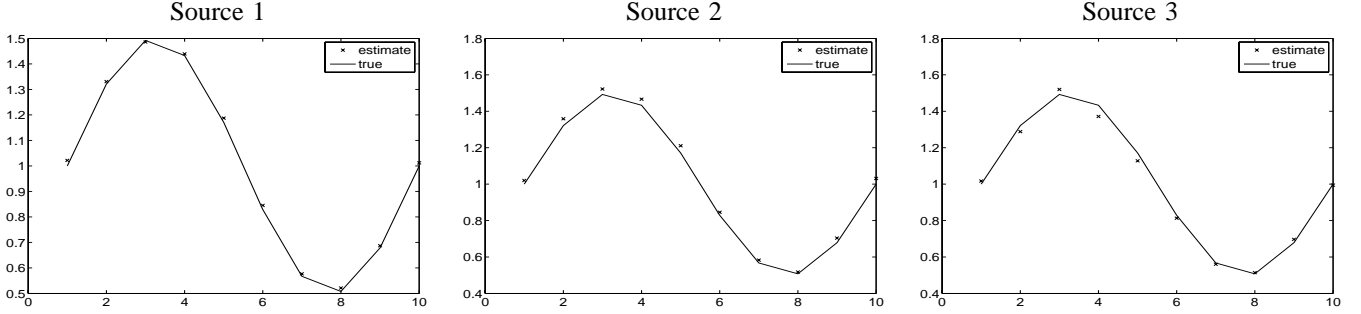


Fig. 1. Evolution of scale factors over time. Straight lines correspond to the true scale factors; estimates are displayed using crosses. The joint method provides a good estimate of the true scale factors without prior knowledge on their values.

detecting pixels whose value differ from the mean of the data by more than 5 times the standard deviation. These pixels are then replaced by a surrogate pixel whose value is computed using a median filter.

We proceed to run the separate and joint unmixing strategies on the data set. Separate unmixing is again carried out using the default parameters. The parameters of the proposed joint unmixing algorithm are initialized in the following way:

- the initial abundance maps for the background endmembers, resp. denoted by 'mountain', 'sand' and 'sky', are set to the three maps extracted separately from the first image (prior to the appearance of the gas plume) using MVSA and SUNSAL. The initial abundance maps for the gas plume are matched to a segmentation of the plume (*i.e.* a series of binary images where each pixel is either classified as belonging to the plume or not), known beforehand [38];
- we obtain the reference spectra matrix S_0 by performing nonnegative least squares inversion on matrix A_5^{init} (the time index being selected arbitrarily among all frames containing all four endmembers);
- higher regularization parameters are set for the first three sources to enforce slower dynamics.

The running times of both separate and joint unmixing methods are resp. 7 min and 44 min for the whole data set. Comparatively, nonlinear unmixing using the PPNMM takes approximately ten hours. The results are displayed in Figures 6, 7, 8 and 9.

The SU results on the first time frame show a discrepancy between the 'separate' and 'joint' method. The 'sand' endmember seems correctly extracted in both cases, but the abundance maps of the 'mountain' and 'sky' endmembers indicate that the 'joint' method unmixes them better than the 'separate' method. Conversely, a 'ghost' of the spatial support of the gas

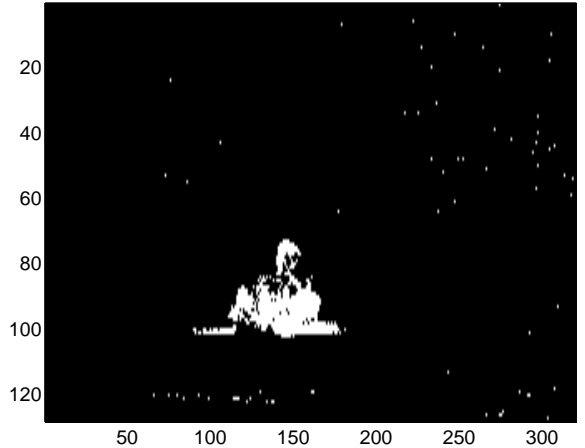


Fig. 3. Spatial display of the binary detection test result for each pixel of the third time frame, using a general likelihood ratio on the value of the estimated nonlinearity parameter. A value of one (white) indicates a nonlinear mixing process, a value of 0 (black) corresponds to the LMM. As can be seen, the LMM mainly fails to hold within the spatial support of the gas plume, isolated pixels corresponding to remaining outliers in the scene. Anywhere else, the LMM can be assumed to be a good approximation of the actual physical mixing process.

plume within all time frames can be observed on the three abundance maps produced by the 'joint' unmixing method on the current time frame. Removing this artefact caused by the proposed ALS implementation is one of the perspective of this work. The next time frames display a common extraction pattern: as expected, standard linear unmixing fails within the spatial support of the plume. Spectrally, it does seem that the gas is correctly attributed to a single endmember whose index varies along the time frames because of the

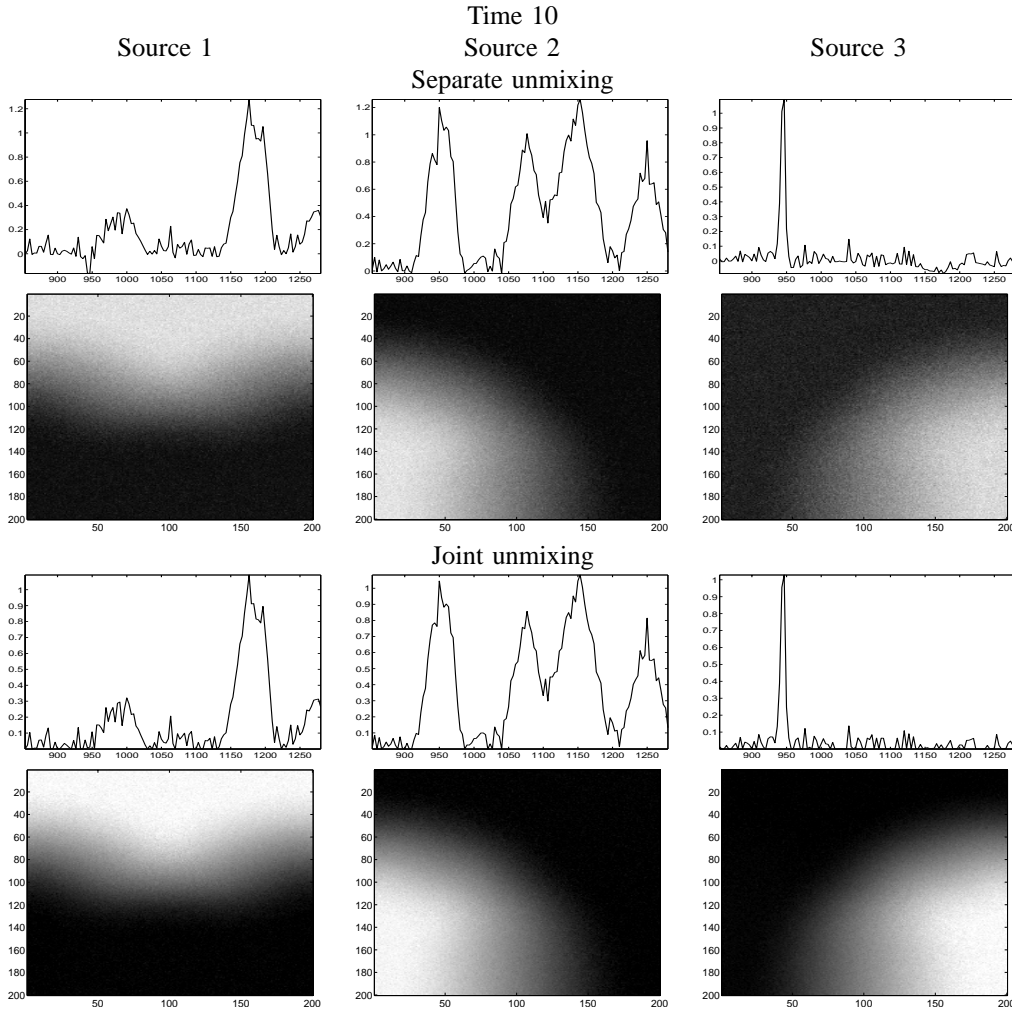


Fig. 2. Unmixing of the tenth time frame. Each column corresponds to a particular endmember. The first and second row resp. display the spectra and abundance maps estimated by the separate approach, while the third and fourth row present the results of the joint approach. Both methods yield visually similar performances.

permutation problem. However, the bad fit of the LMM in this spatial region causes the gas plume to appear on all four estimated abundance maps. Conversely, accounting for the temporal information in the joint unmixing approach allows to assign the gas plume to a single endmember (the fourth one).

Spectral scale factors estimated by the joint unmixing method are displayed as a function of time in figure 5. The first three plots correspond to the natural endmembers in the scene - 'sky', 'mountain', 'sand' - and show very small perturbations around the unity value. Hence, the dynamics of these three endmembers can almost be considered as constant. The scale factor plot for the gas plume endmember displays a different pattern: the curve peaks at the third time frame, then slowly decays with time. Since the scale factor in endmember variability is linked to illumination properties of the material, the plot may be interpreted as the density of the plume, peaking just after the release then decreasing when the gas expands.

As a final note, we point out that the unmixing results are not obtained by relying solely on the proposed model.

Indeed, we exploit a segmentation of this data set to perform the initialization step, which allows to avoid 'bad' local minima of the objective function [38]. When less information about the data is available beforehand, a possible approach is to resort to multiple initializations in order to tackle the non convex nature of the problem, at the cost of a greater computational complexity. In the following experiment, the proposed algorithm is run with all abundance maps initialized as constant images. Figure 10 displays the results obtained by the algorithm on the fourth time frame. As shown in the fourth panel of the figure, the gas plume is correctly extracted without using any segmentation technique. Other time frames are less physically interpretable, perhaps indicating that the method is stuck in a local minimum of the objective function. In the proposed strategy, the fourth time frame can then be used as a better initialization. We conclude from figure 10 that the dynamical monitoring of the sources and abundances lead to promising results in multitemporal spectral unmixing.

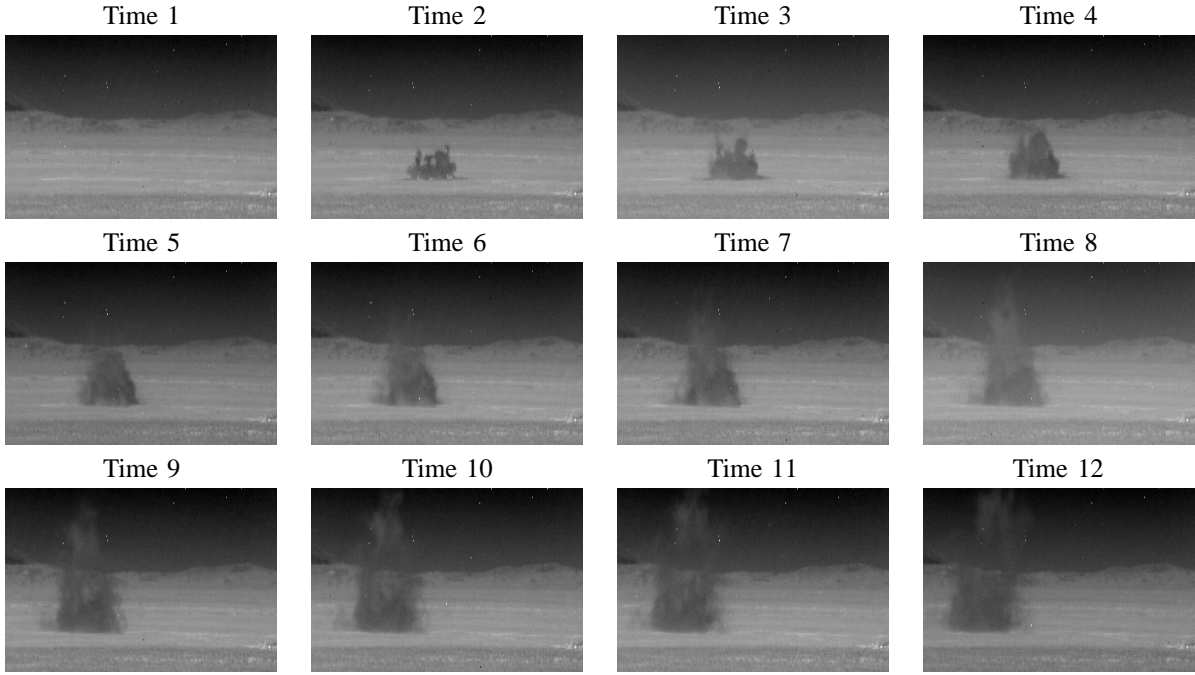


Fig. 4. First principal component of each time frame: the sequence depicts the evolution of the gas plume in the scene over time.

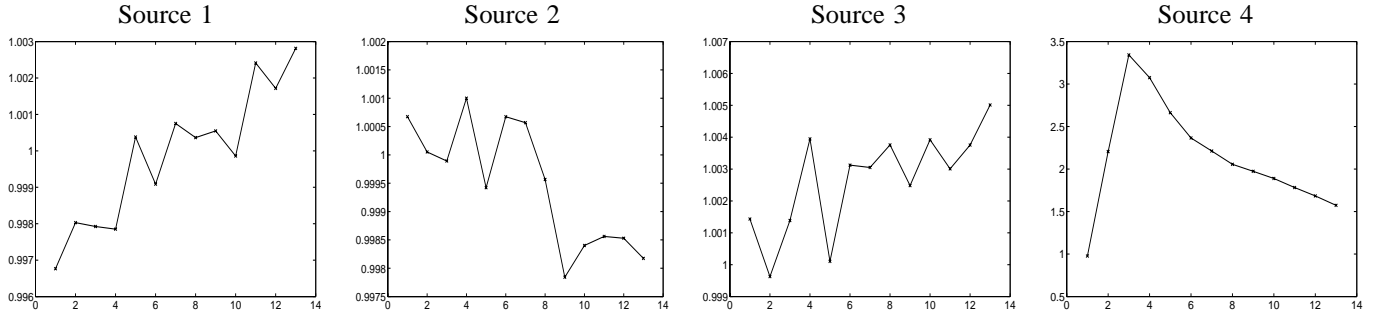


Fig. 5. Evolution of scale factors over time : each plot corresponds to a particular endmember. Notice how the first three plots - 'sky', 'mountain', 'sand' - display tiny variations around unity, of the order of 10^{-3} , whereas the fourth plot - gas plume- can be explained by the dynamical variation of the density of the plume.

V. CONCLUSION

In this paper, we have proposed a general dynamical framework for spectral unmixing:

$$\begin{cases} \mathbf{X}_k &= \mathbf{S}_k \mathbf{A}_k + \mathbf{E}_k \\ \mathbf{S}_k &= f_S(\mathbf{S}_{k-1}) + \mathbf{V}_k \\ \mathbf{A}_k &= f_A(\mathbf{A}_{k-1}) + \mathbf{D}_k. \end{cases}$$

The linear mixing model is assumed to hold at each time frame to benefit from the low computational complexity of linear unmixing methods. We make assumptions on the dynamics of the spectral signatures and abundance coefficients of sources, rather than on the data themselves, and hence fall within a data-driven framework. We propose a simplified version of this model tailored to the case of multitemporal hyperspectral images. We derive an efficient unmixing algorithm based on this model, which jointly processes all time frames in the image. The proposed method relies on an efficient non-negative alternating least squares scheme. The performance of our approach is demonstrated on synthetic and real time series of hyperspectral images. We are currently investigating the

extension of the method to account for more complex spectral variability schemes, in the temporal dimension as well as the spatial dimension of the image. Perspectives also include the extension of the model to nonlinear mixing processes. Finally, it is worth noting that the general dynamical framework is not restricted to the case of hyperspectral imaging. Because of its flexibility, it allows to analyze the dynamics of many types of multidimensional signals, *e.g.* biomedical signals such as electroencephalography (EEG) or magnetoencephalography (MEG).

ACKNOWLEDGMENT

This work was supported by the European Research Council project CHESS, under Grant 2012-ERC-AdG-320684 and by DGA under Grant 2015 60 0012 00.470.75.01. We thank Andrea Bertozzi, Department of Mathematics, University of California - Los Angeles (UCLA), for her collaboration on the dataset provided by the US Defense Threat Reduction Agency and the National Science Foundation through NSF Grant DMS-1118971. This work was also partially funded through DGA, under grant 2015-60-001200.470.75.01.

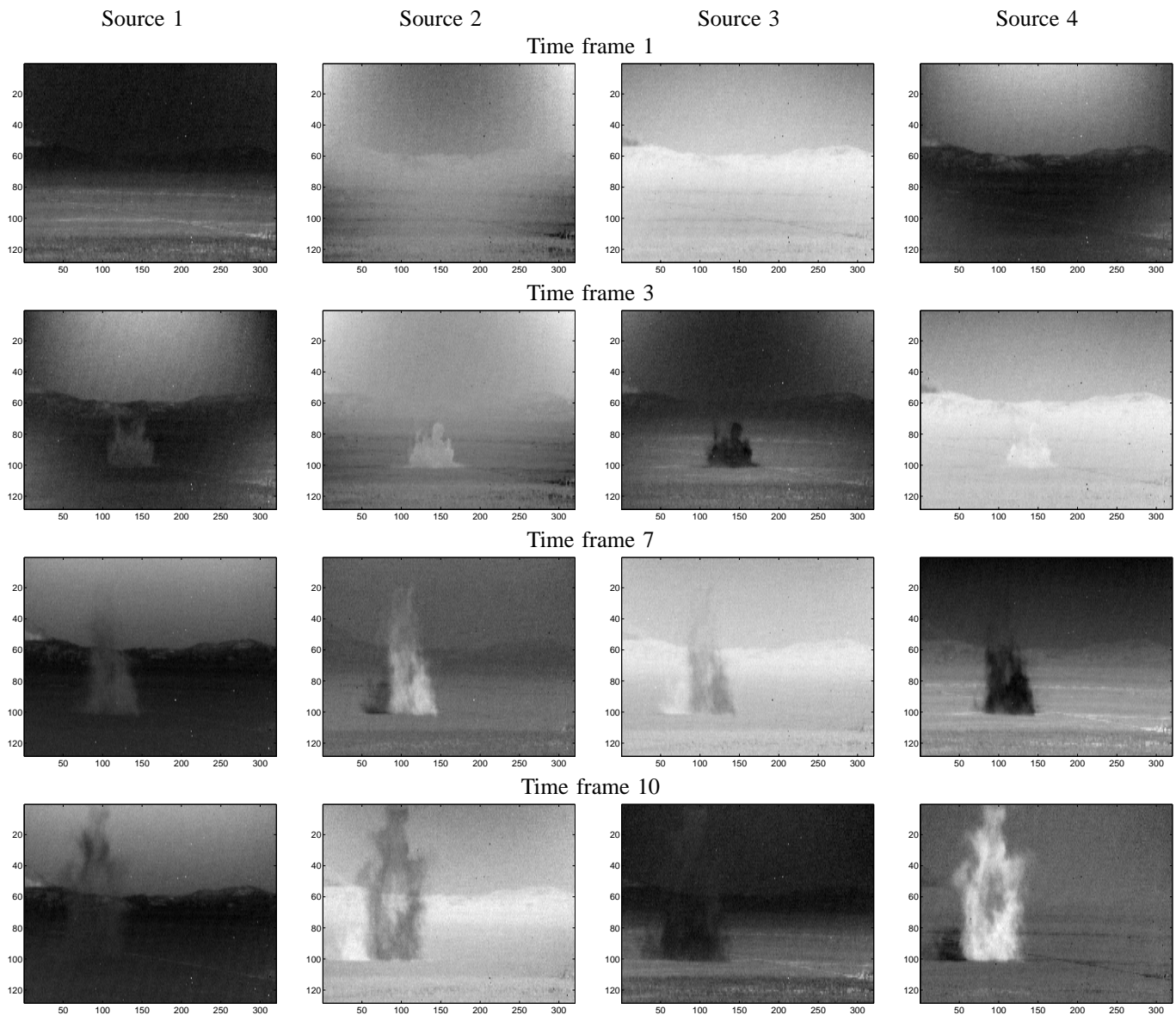


Fig. 6. Abundance maps obtained by the separate unmixing method : estimated abundance maps of the first, third, seventh and tenth time frame. Each row corresponds to a time frame and each column to a particular source. After occurrence of the gas plume, 'ghosts' corrupt all extracted abundance maps: the gas plume cannot be uniquely attributed to any endmember, preventing a clear physical interpretation of the maps.

REFERENCES

- [1] Nirmal Keshava and John F Mustard, "Spectral unmixing," *Signal Processing Magazine, IEEE*, vol. 19, no. 1, pp. 44–57, 2002.
- [2] J.M. Bioucas-Dias, A. Plaza, N. Dobigeon, M. Parente, Qian Du, P. Gader, and J. Chanussot, "Hyperspectral unmixing overview: Geometrical, statistical, and sparse regression-based approaches," *IEEE Journal of Selected Topics in Applied Earth Observations and Remote Sensing*, vol. 5, no. 2, pp. 354–379, april 2012.
- [3] J. Chen, C. Richard, and P. Honeine, "Nonlinear unmixing of hyperspectral data based on a linear-mixture/nonlinear-fluctuation model," *IEEE Transactions on Signal Processing*, vol. 61, no. 2, pp. 480–492, 2013.
- [4] N. Dobigeon, J.-Y. Tournet, C. Richard, J.C.M. Bermudez, S. McLaughlin, and A.O. Hero, "Nonlinear unmixing of hyperspectral images: Models and algorithms," *Signal Processing Magazine, IEEE*, vol. 31, no. 1, pp. 82–94, Jan 2014.
- [5] N.H. Nguyen, C. Richard, P. Honeine, and C. Theys, "Hyperspectral image unmixing using manifold learning methods derivations and comparative tests," in *IEEE International Geoscience and Remote Sensing Symposium (IGARSS)*. IEEE, 2012, pp. 3086–3089.
- [6] D. Lungu, S. Prasad, M.M. Crawford, and O. Ersoy, "Manifold-learning-based feature extraction for classification of hyperspectral data: A review of advances in manifold learning," *IEEE Signal Processing Magazine*, vol. 31, no. 1, pp. 55–66, 2014.
- [7] E. Merkurjev, J. Sunu, and A.L. Bertozzi, "Graph mbo method for multiclass segmentation of hyperspectral stand-off detection video," in *2014 IEEE International Conference on Image Processing ICIP*. IEEE, 2014, pp. 689–693.
- [8] H. Hu, J. Sunu, and A.L. Bertozzi, "Multi-class graph mumford-shah model for plume detection using the mbo scheme," in *Energy Minimization Methods in Computer Vision and Pattern Recognition*. Springer, 2015, pp. 209–222.
- [9] D. Tuia, M. Trollet, and M. Volpi, "Multisensor alignment of image manifolds," in *IEEE International Geoscience and Remote Sensing Symposium (IGARSS)*, 2013, pp. 1246–1249.
- [10] H.L. Yang and M.M. Crawford, "Manifold alignment for multitemporal hyperspectral image classification," in *IEEE International Geoscience and Remote Sensing Symposium (IGARSS)*. IEEE, 2011, pp. 4332–4335.
- [11] L. Ma, M.M. Crawford, and J. Tian, "Local manifold learning-based-nearest-neighbor for hyperspectral image classification," *IEEE Transactions on Geoscience and Remote Sensing*, vol. 48, no. 11, pp. 4099–4109, 2010.
- [12] H.L. Yang and M.M. Crawford, "Learning a joint manifold with global-

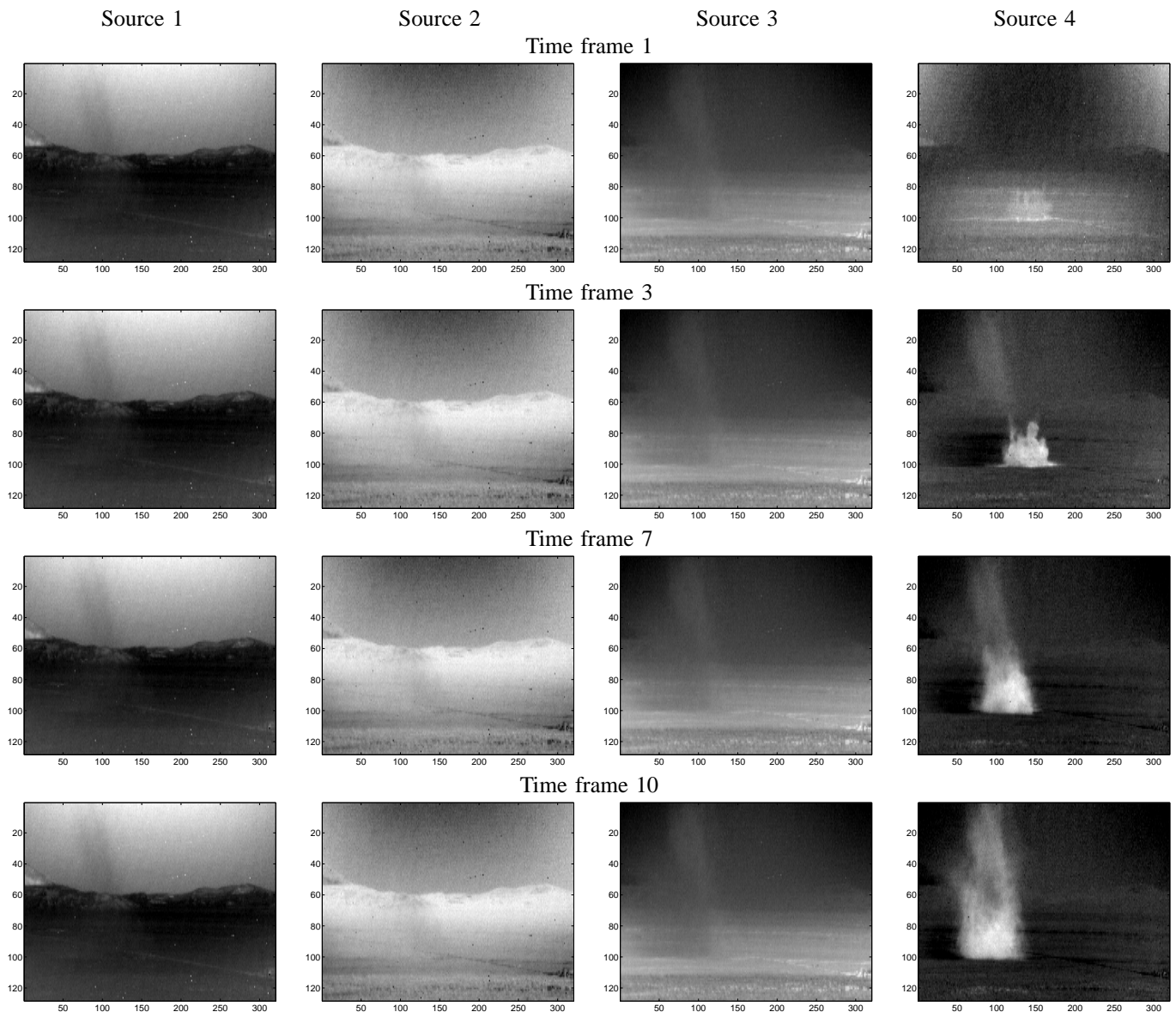


Fig. 7. Abundance maps obtained by the joint unmixing method : estimated abundance maps of the first, third, seventh and tenth time frame. Each row corresponds to a time frame and each column to a particular source. Notice how 'ghosts' are significantly attenuated by accounting for the dynamical model of the data: abundances of sources 1 to 3 are barely corrupted by gas-plume related information (source 4).

- local preservation for multitemporal hyperspectral image classification," in *IEEE International Geoscience and Remote Sensing Symposium (IGARSS)*, 2013, pp. 1047–1050.
- [13] M.-D. Iordache, L. Tits, J.M. Bioucas-Dias, A. Plaza, and B. Somers, "A dynamic unmixing framework for plant production system monitoring," *Selected Topics in Applied Earth Observations and Remote Sensing, IEEE Journal of*, vol. 7, no. 6, pp. 2016–2034, June 2014.
 - [14] C.-I. Chang and Q. Du, "Estimation of number of spectrally distinct signal sources in hyperspectral imagery," *IEEE Transactions on Geoscience and Remote Sensing*, vol. 42, no. 3, pp. 608–619, 2004.
 - [15] J.M. Bioucas-Dias and J.M.P. Nascimento, "Hyperspectral subspace identification," *IEEE Transactions on Geoscience and Remote Sensing*, vol. 46, no. 8, pp. 2435–2445, Aug 2008.
 - [16] B. Luo, J. Chanussot, S. Doute, and L. Zhang, "Empirical automatic estimation of the number of endmembers in hyperspectral images," *IEEE Geoscience and Remote Sensing Letters*, vol. 10, no. 1, pp. 24–28, Jan 2013.
 - [17] G.A. Shaw and H.-H.K. Burke, "Spectral imaging for remote sensing," *Lincoln Laboratory Journal*, vol. 14, no. 1, pp. 3–28, 2003.
 - [18] J.M.P. Nascimento and J.M. Bioucas Dias, "Does independent component analysis play a role in unmixing hyperspectral data?," *IEEE Transactions on Geoscience and Remote Sensing*, vol. 43, no. 1, pp. 175–187, 2005.
 - [19] T.A. Scambos, M.J. Dutkiewicz, J.C. Wilson, and R.A. Bindshadler, "Application of image cross-correlation to the measurement of glacier velocity using satellite image data," *Remote Sensing of Environment*, vol. 42, no. 3, pp. 177–186, 1992.
 - [20] J. Chen, C. Richard, and P. Honeine, "Nonlinear estimation of material abundances in hyperspectral images with-norm spatial regularization," *IEEE Transactions on Geoscience and Remote Sensing*, vol. 52, no. 5, pp. 2654–2665, 2014.
 - [21] A. Cichocki, R. Zdunek, A.H. Phan, and S.-I. Amari, *Nonnegative matrix and tensor factorizations: applications to exploratory multi-way data analysis and blind source separation*, John Wiley & Sons, 2009.
 - [22] R.E. Kalman, "A new approach to linear filtering and prediction problems," *Journal of Fluids Engineering*, vol. 82, no. 1, pp. 35–45, 1960.
 - [23] A. Zare and K. Ho, "Endmember variability in hyperspectral analysis: Addressing spectral variability during spectral unmixing," *IEEE Signal Processing Magazine*, vol. 31, no. 1, pp. 95–104, 2014.
 - [24] D.A. Roberts, M. Gardner, R. Church, S. Ustin, G. Scheer, and R.O. Green, "Mapping chaparral in the Santa Monica mountains using

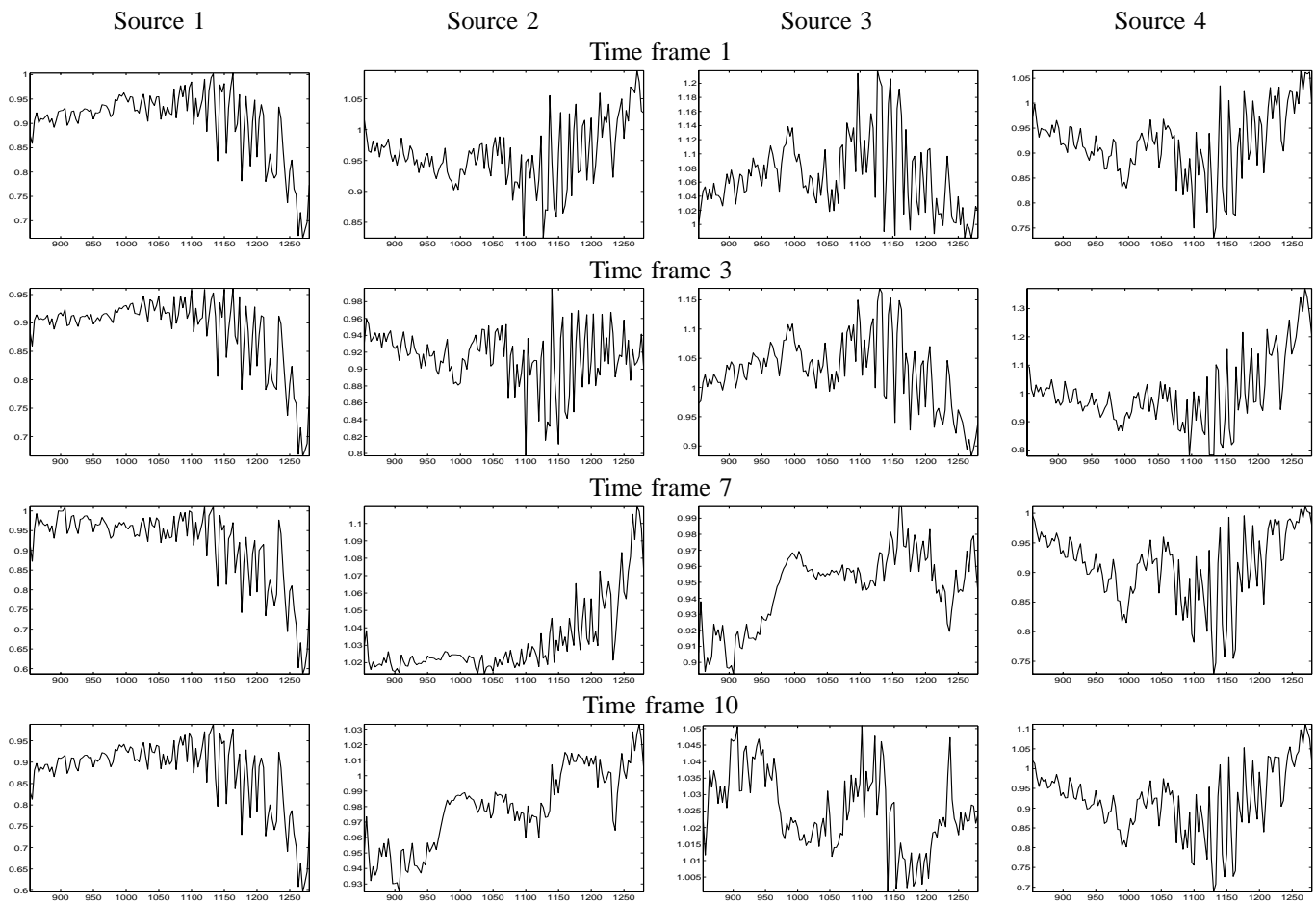


Fig. 8. Endmembers obtained by the separate unmixing method : estimated spectra from the first, third, seventh and tenth time frame. Each row corresponds to a time frame and each column to a particular source. The larger the contribution of the 'ghost' to a specific abundance map, the larger the distortion of the corresponding extracted endmember: see e.g. the seventh and tenth time frames of source 2 and 3.

- multiple endmember spectral mixture models," *Remote Sensing of Environment*, vol. 65, no. 3, pp. 267–279, 1998.
- [25] A. Halimi, N. Dobigeon, J.-Y. Tourneret, and P. Honeine, "A new Bayesian unmixing algorithm for hyperspectral images mitigating end-member variability," in *2015 IEEE International Conference on Acoustics, Speech and Signal Processing (ICASSP)*, April 2015, pp. 2469–2473.
- [26] Y. Song, D. Brie, E.-H. Djermoune, and S. Henrot, "Minimum distance criterion for non-negative hyperspectral image deconvolution," Research report, CRAN, Sept. 2015.
- [27] M.W. Berry, M. Browne, A.N. Langville, V.P. Pauca, and R.J. Plemmons, "Algorithms and applications for approximate nonnegative matrix factorization," *Computational Statistics & Data Analysis*, vol. 52, no. 1, pp. 155–173, 2007.
- [28] A. Cichocki and R. Zdunek, "Regularized alternating least squares algorithms for non-negative matrix/tensor factorization," in *Advances in Neural Networks-ISNN 2007*, pp. 793–802. Springer, 2007.
- [29] S. Boyd, N. Parikh, E. Chu, B. Peleato, and J. Eckstein, "Distributed optimization and statistical learning via the alternating direction method of multipliers," *Foundations and Trends® in Machine Learning*, vol. 3, no. 1, pp. 1–122, 2011.
- [30] J.M.P. Nascimento and J.M. Bioucas Dias, "Vertex component analysis: A fast algorithm to unmix hyperspectral data," *IEEE Transactions on Geoscience and Remote Sensing*, vol. 43, no. 4, pp. 898–910, 2005.
- [31] J. Li and J.M. Bioucas-Dias, "Minimum volume simplex analysis: A fast algorithm to unmix hyperspectral data," in *Geoscience and Remote Sensing Symposium, 2008. IGARSS 2008. IEEE International. IEEE*, 2008, vol. 3, pp. III–250.
- [32] D.C. Heinz and C.-I. Chang, "Fully constrained least squares linear spectral mixture analysis method for material quantification in hyperspectral imagery," *IEEE Transactions on Geoscience and Remote Sensing*, vol. 39, no. 3, pp. 529–545, 2001.
- [33] N. Gillis, "Sparse and unique nonnegative matrix factorization through data preprocessing," *The Journal of Machine Learning Research*, vol. 13, no. 1, pp. 3349–3386, 2012.
- [34] S. Moussaoui, D. Brie, and J. Idier, "Non-negative source separation: range of admissible solutions and conditions for the uniqueness of the solution," in *Acoustics, Speech, and Signal Processing, 2005. Proceedings (ICASSP'05). IEEE International Conference on. IEEE*, 2005, vol. 5, pp. v–289.
- [35] J.M. Bioucas-Dias and M.A.T. Figueiredo, "Alternating direction algorithms for constrained sparse regression: Application to hyperspectral unmixing," in *Hyperspectral Image and Signal Processing: Evolution in Remote Sensing (WHISPERS), 2010 2nd Workshop on. IEEE*, 2010, pp. 1–4.
- [36] J.B. Broadwater, D. Limsui, and A.K. Carr, "A primer for chemical plume detection using LWIR sensors," Tech. Rep., National Security Technology Department, 2011.
- [37] Y. Altmann, N. Dobigeon, and J.-Y. Tourneret, "Nonlinearity detection in hyperspectral images using a polynomial post-nonlinear mixing model," *Image Processing, IEEE Transactions on*, vol. 22, no. 4, pp. 1267–1276, 2013.
- [38] G. Tochon, J. Chanussot, J. Gilles, M. Dalla Mura, J.-M. Chang, and A.L. Bertozzi, "Gas plume detection and tracking in hyperspectral video sequences using binary partition trees," in *IEEE Workshop on Hyperspectral Image and Signal Processing: Evolution in Remote Sensing (WHISPERS 2014)*, 2014.

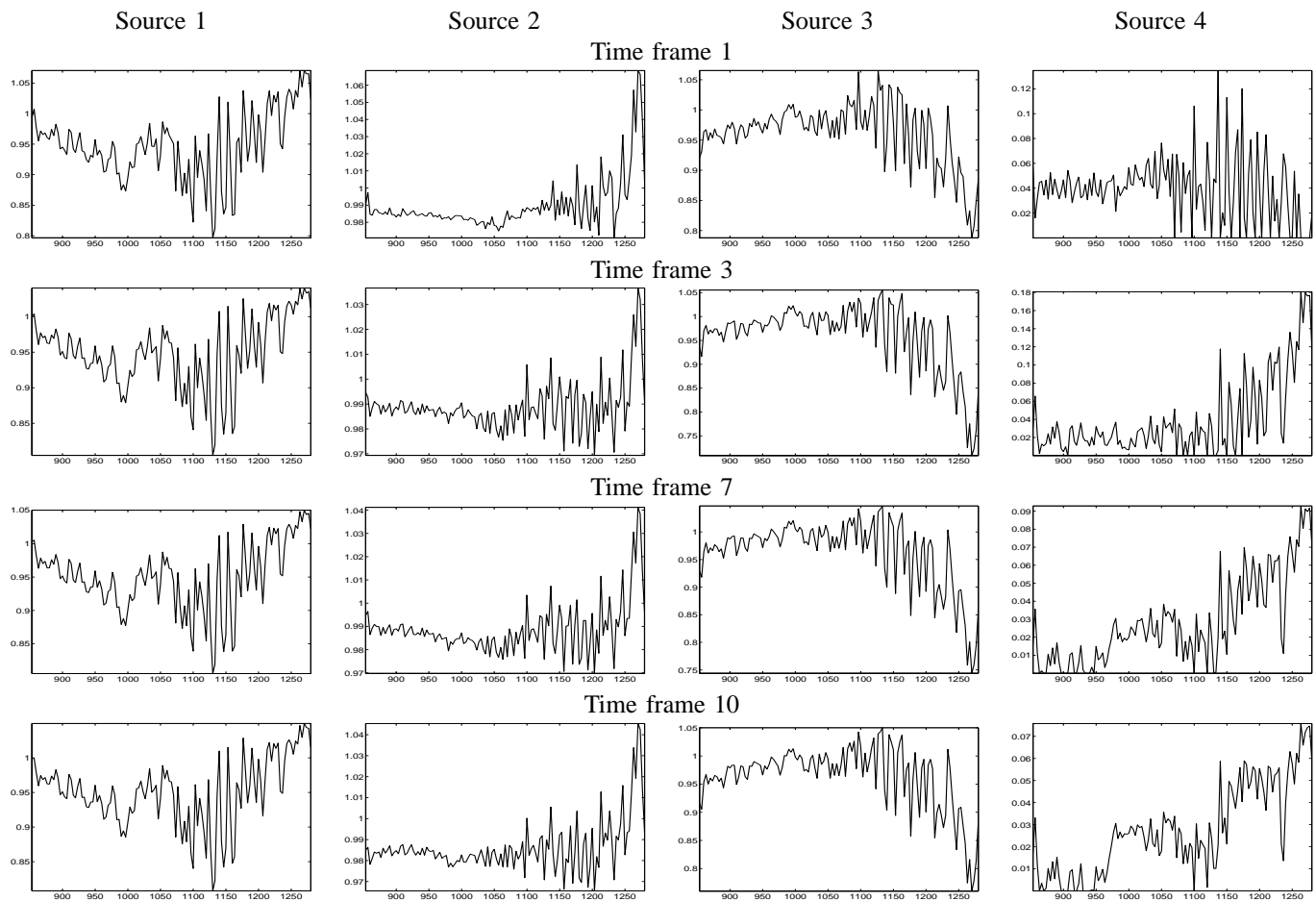


Fig. 9. Endmembers obtained by the joint unmixing method : estimated spectra from the first, third, seventh and tenth time frame. Each row corresponds to a time frame and each column to a particular source. Notice how all spectra fit the proposed model of the data.



Simon Henrot was born in France in 1986. He graduated in electrical engineering from the Ecole Nationale de l'Aviation Civile, Toulouse, France in 2009 and received the Ph.D. degree in signal processing from the Université de Lorraine, Nancy, France in 2013. He is currently a post-doctoral student with Université Joseph Fourier, Grenoble, France at the Grenoble Images Speech Signals and Automatics Laboratory (GIPSA-Lab). His research interest include inverse problems in imaging and multimodal image processing.



Jocelyn Chanussot (M04SM04F12) received the M.Sc. degree in electrical engineering from the Grenoble Institute of Technology (Grenoble INP), Grenoble, France, in 1995, and the Ph.D. degree from the Université de Savoie, Annecy, France, in 1998. In 1999, he was with the Geography Imagery Perception Laboratory for the Delegation Generale de l'Armement (DGA - French National Defense Department). Since 1999, he has been with Grenoble INP, where he was an Assistant Professor from 1999 to 2005, an Associate Professor from 2005 to

2007, and is currently a Professor of signal and image processing. He is conducting his research at the Grenoble Images Speech Signals and Automatics Laboratory (GIPSA-Lab). His research interests include image analysis, multicomponent image processing, nonlinear filtering, and data fusion in remote sensing. He has been a visiting scholar at Stanford University (USA), KTH (Sweden) and NUS (Singapore). Since 2013, he is an Adjunct Professor of the University of Iceland. In 2015-2017, he is a visiting professor at the University of California, Los Angeles (UCLA). Dr. Chanussot is the founding President of IEEE Geoscience and Remote Sensing French chapter (2007-2010) which received the 2010 IEEE GRSS-S Chapter Excellence Award. He was the co-recipient of the NORSIG 2006 Best Student Paper Award, the IEEE GRSS 2011 and 2015 Symposium Best Paper Award, the IEEE GRSS 2012 Transactions Prize Paper Award and the IEEE GRSS 2013 Highest Impact Paper Award. He was a member of the IEEE Geoscience and Remote Sensing Society AdCom (2009-2010), in charge of membership development. He was the General Chair of the first IEEE GRSS Workshop on Hyperspectral Image and Signal Processing, Evolution in Remote sensing (WHISPERS). He was the Chair (2009-2011) and Cochair of the GRS Data Fusion Technical Committee (2005-2008). He was a member of the Machine Learning for Signal Processing Technical Committee of the IEEE Signal Processing Society (2006-2008) and the Program Chair of the IEEE International Workshop on Machine Learning for Signal Processing, (2009). He was an Associate Editor

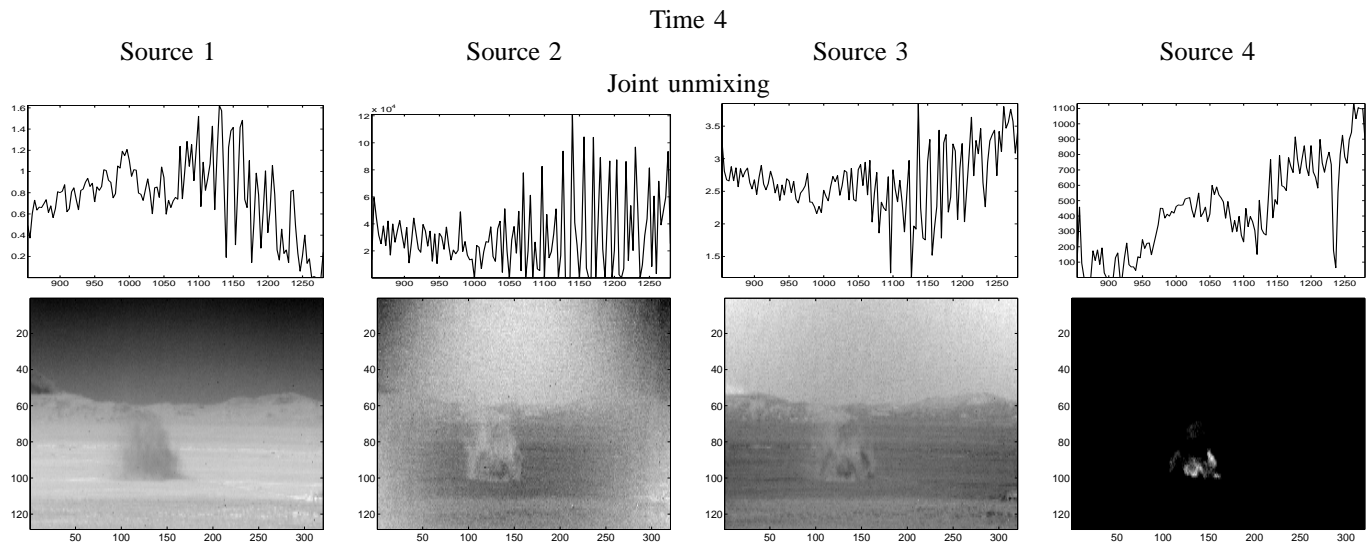


Fig. 10. Unmixing of the fourth time frame with abundance maps initialized as constant images, using the 'joint unmixing' approach. Each column corresponds to a source, the first row displays the extracted spectra and the second row the estimated abundance maps. The joint method correctly attributes the gas plume to a unique endmember (the fourth one) even in the absence of any spatial prior knowledge of the scene.

for the IEEE Geoscience and Remote Sensing Letters (2005-2007) and for Pattern Recognition (2006-2008). Since 2007, he is an Associate Editor for the IEEE Transactions on Geoscience and Remote Sensing. He was the Editor-in-Chief of the IEEE Journal of Selected Topics in Applied Earth Observations and Remote Sensing (2011-2015). In 2013, he was a Guest Editor for the Proceedings of the IEEE and in 2014 a Guest Editor for the IEEE Signal Processing Magazine. He is a Fellow of the IEEE and a member of the Institut Universitaire de France (2012-2017).



Christian Jutten received the PhD degree in 1981 and the Docteur s Sciences degree in 1987 from the Institut National Polytechnique of Grenoble (France). He taught as associate professor in the Electrical Engineering Department from 1982 to 1989, before becoming full professor in University Joseph Fourier of Grenoble, now University Grenoble-Alpes. He was visiting professor in Swiss Federal Polytechnic Institute in Lausanne in 1989 and in Campinas University (Brazil) in 2010. He has been deputy director of the Grenoble images, speech,

signal and control laboratory (GIPSA, 300 people) and head of the Department Images-Signal (DIS, 100 people) from 2007 to 2010. For more than 30 years, his research interests are source separation, independent component analysis, including theoretical aspects (separability, source separation in nonlinear mixtures, sparsity) and applications in signal processing (biomedical, seismic, hyperspectral imaging, speech), and more recently dictionary learning and sparse representations. He is co-author of more than 90 papers in international journals, 4 books, 27 invited plenary talks and 180 communications in international conferences. He has been associate editor of IEEE Trans. on Circuits and Systems (1994-95) and is currently handling editor of Signal Processing. He was the co-organizer the 1st International Conference on Blind Signal Separation and Independent Component Analysis (Aussois, France, 1999). He has been a scientific advisor for signal and images processing at the French Ministry of Research in 1996-98 and for the French National Research Center (CNRS) in 2003-06. He was deputy director of Institute for Information Sciences and Technologies of CNRS from May 2012 to September 2014 and is still scientific advisor for CNRS in signal and image processing area. He received the Medal Blondel in 1997 from SEE (French Electrical Engineering society) for his contributions in source separation and independent component analysis. He has been elevated as IEEE fellow (2008) and EURASIP Fellow (2013) and nominated for 5 years as a senior member of Institut Universitaire de France in 2008 with renewal in 2013. In 2012, he was awarded by an ERC Advanced Grant: CHallenges in Extraction and Separation of Sources (CHESS).